Journal of Materials Chemistry C

Accepted Manuscript

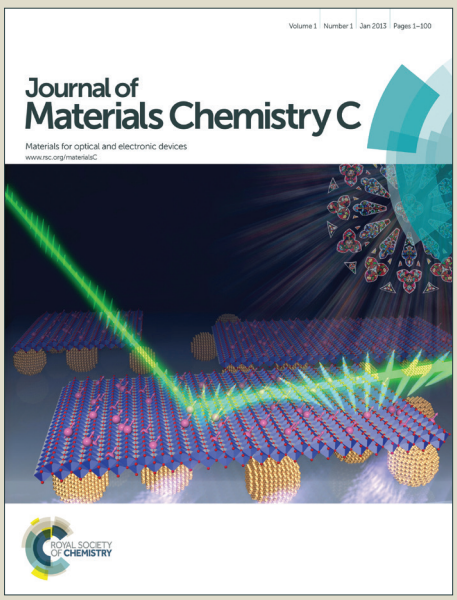

ROYAL SOCIETY OF CHEMISTRY

www.rsc.org/materialsC

Controlled Hybridization of Sn-SnO_2 Nanoparticles via Simple-Programmed Microfluidic Processes for Tunable Ultraviolet and Blue Emissions

Shuai Li,[1$] Xiaodi Zhong,[1$] Yujun Song,[2*, 1] Jiaguang Sun,[1] Xiaomiao Shen,[1] Yuanjun Song,[3] Rongming Wang,[2*, 3] Min Zhu,[4] Haizheng Zhong[4] and Aiguo Zheng[5]

[1]School of Materials Science and Engineering, Beihang University, Beijing 100191, China; [2]School of Mathematics and Physics, University of Science and Technology Beijing, Beijing 100083, China; [3]Department of Physics, Beihang University, Beijing 100191, China; [4]School of Materials Sciences and Engineering, Beijing Institute of Technology, Beijing 100181, China; [5]Institute of Petroleum Science and Technology of China, Beijing 100088, China

Correspondence and requests for materials should be addressed to Y.S.: songyj@buaa.edu.cn; R.W.: rmwang@buaa.edu.cn

Abstract

Precisely controlling microstructure and composition of each component in hybrid nanomaterials is critical for desired properties but very challenging. Herein, we demonstrate a new proof-of-concept method, or microtubing-based simple-programmed microfluidic processes (MT-SPMPs). MT-SPMPs preserve the ability for controlled hybridization by accurately adjusting the detailed microstructures and crystal phases of components using Sn-SnO_2 nanoparticles as models, by coupling the synergistic effects of complex surfactants with the precise reaction kinetics control. Consequently, uniform Sn-SnO_2 nanospheres with diameters from 2 nm to 14 nm or Sn@SnO_2 nanorods with diameter of 19 nm, length of 66 nm can be achieved. The SnO_2 shell thickness can be well controlled at the Bohr exciton radius range. Particularly, the defect type and density in these nanospheres and nanorods can be tuned for unique ultraviolet emission at 347 nm or enhanced blue emission at 475 nm. Analysis on the detailed microstructure and crystal-phase dependent photoluminescences indicates that the quantum mechanical dipole-forbidden rule can be effectively conquered by the formation of Sn-SnO_2 nanohybrids with controlled defects (oxygen vacancies or Sn interstitials).

Key words: Nanohybrid, Sn-SnO_2, Ultraviolet emission, Blue emission, Microstructure control

Introduction

Metal oxides are an important group of materials because they form a wide variety of structures, display many interesting physicochemical properties and have numerous technological applications.[1-5] Among them, tin oxide (SnO_2) is extremely promising as an intrinsic n-type oxide semiconductor with good chemical and mechanical stability,[6] a wide bandgap of 3.6 eV at 300 K,[6] a highly achievable carrier concentration up to 6×10^{20}/cm,[3 7] and an exciton-binding energy of 130 meV larger than those of ZnO (60 meV) and GaN (25 meV).[8,9] SnO_2 nanostructures have shown potential use in sensors,[10,11] transistors,[12-14] light-emitting diodes,[15,16] photovoltaic cells,[17] photo-catalysis[18] and lithium batteries.[19-21] However, the even-parity symmetry of the conduction-band minimum and valence-band maximum states in SnO_2 prohibits the band-edge radiative transition and light emission,[22] which hinders their further application in optoelectronic devices, such as ultraviolet (UV) light emitters.[8,9]

Recent investigation indicates that the defect-induced electronic states near the band edges can be tuned effectively via hybridization of SnO_2 by introduction of a second metallic component or mixed crystalline and amorphous phases at nanoscale to achieve enhanced quantum-confinement effect.[23,24] Consequently, their band structures, in particular the symmetry of band-edge quantum states, can be conveniently modified to realize band-edge radiative transition and UV light emission.[23,25,26] However, it is very challenging to synthesize free nanoparticles (NPs) with unequivocal quantum-size effects and controlled defects since most current processes suffer from difficulties in fabricating the desired hybrid nanostructures and/or controlling sizes at the exciton Bohr radius of SnO_2 (~2.7 nm).[25-29] The overgrown sizes and out-of-control of microstructures in SnO_2 NPs usually lead to asymmetric, broad and/or multiplex emissions in the optical range.[23,24,30-32] UV emissions at room temperature were only observed in some hybrid SnO_2 nanostructures, such as the thin film with SnO_2 nanocrystals doping in the amorphous matrix excited by the 325 nm laser line,[23] the 100 nm SnO_2 nanowires coated with amorphous shells of ~1.5 nm thick excited at the 355 nm wavelength,[33] the 100-200

nm SnO_2 nanowires confined on p-type silicon wafers excited at the 325 nm laser line.[34]

We have invented an *in situ* rapidly cooling and multi-step microfluidic process[35-41] and an *in situ* redox microfluidic process[42] for size and structure-controlled nanoparticle synthesis. Particularly, amorphous Fe(B)@Fe_3O_4 (Fe(B): boron-doped iron) with uniform shell thickness about 2 nm can be synthesized at large scale.[42] We further developed microtubing-based simple-programmed microfluidic processes (MT-SPMPs), which exhibit precise spatiotemporal kinetics control at each stage during the nanoparticle formation. Our research on the synthesis of NPs by wet-chemical process also revealed that the growth of well-dispersed NPs depended not only on the reaction kinetic parameter (temperature, pressure, reactant concentrations, flow rates and flow types for continuous flow process, or stirring speeds for bottle-batched process, etc.) control but also on the interaction between stabilizers and surfaces of the NPs (e.g., the binding types and strengths between stabilizers and surfaces of NPs). Thus, a complex stabilizing system including polyvinylpyrrolidone (PVP), maleic anhydride (MAH) and sodium citrate (TSC) was developed for well-dispersed NPs with good size control, exhibiting a synergistic effect in the dispersion stabilization and size control of NPs.[42,43] Herein, we try to extend these progresses to a new concept-of-proof synthesis strategy by coupling the synergistic effects of the complex surfactants with the precise spatiotemporal kinetics control in MT-SPMPs. Using the synthesis of Sn-SnO_2 nanohybrids (mixed Sn and SnO_2 in single NPs) and Sn@SnO_2 NPs (briefly Sn(-/@)SnO_2) as models, MT-SPMPs show versatility in morphology and structure control for desired properties. Consequently, Sn@SnO_2 nanorods and Sn-SnO_2 nanospheres with tunable sizes and crystal phases can be synthesized by adjusting the kinetic parameters of MT-SPMPs and the synergistic effects of stabilizers. The SnO_2 components can be well controlled at the exciton Bohr radius range. These nanohybrids exhibit significant morphology and crystal-structure dependent photoluminescences with unique emission bands centered at 347 nm or 475 nm, which can be well elucidated by the quantum-size effects, interfacial electron-coupling effects between Sn and SnO_2 components, and

defects in SnO_2.

Experiments

Figure 1A shows the typical experiment setup of the MT-SPMPs.[35-37] This setup entails: (1) one syringe pump for the metal-salt solution (e.g., $SnCl_2$ in ultrapure water); (2) one syringe pump for the reducing-agent solution (e.g., $NaBH_4$ in N-methyl-2-pyrrolidone (NMP)); (3-4) two preheating stainless-steel spirals immersed in the thermostatic tank 1 (inner diameter (ID) = 127μm, length (L) = 15 cm) to increase the metal-salt solution and the reducing-agent solution from room temperature to 100°C or higher; (5) one Y-mixer (ID = 250μm, L = 4~5mm) for the reactants to form precursors and then to initiate nucleation; (6) one microtubing spiral (ID = 127~500μm, L = 25~50 cm) in the thermostatic tank 2 with temperature from 0°C to 100°C or higher for finishing nucleation and growth of nanoparticles; and (7) one product receiver protected by inert gas (i.e., N_2), with temperature controlled from -10°C to 100°C or higher by the thermostatic tank 3. Typically, the metal-salt solution is prepared by dissolving $SnCl_2 \cdot 2H_2O$ of 0.32 g (1.42 mmol), polypyrrolidone (PVP) of 0.5 g (Mw = 10000), and/or sodium citrate (TSC) of 3.3 g (11.2 mmol), and/or maleic anhydride (MA) of 0.52 g (5.3 mmol) into 50 mL ultrapure water. The reducing solution is prepared by dissolving $NaBH_4$ of 0.16 g (4.1 mmol) into 50 mL NMP. The Sn-SnO_2 nanohybrids were formed according to the following reactions. First, tin metal NPs are formed by tin salt reduction stabilized by PVP, TSC and maleic acid (MAH) or PVP only, as shown in reaction (rx) 1 with kinetic parameters controlled by MT-SPMPs. Then, some metal atoms, particularly surface-metal atoms in the formed metal-alloy cores, are *in-situ* oxidized into metal oxide (rx 2) in the microfluidic reactor to form metal-metal oxide nanohybrids or metal@metal-oxide NPs. Since lots of $NaBH_4$ and H_2O exist in the reaction system and NMP is a kind of basic solvent, the reaction solution is usually basic, and oxidization of Sn^{2+} to Sn^{4+} by H_2O (rx 3) or disproportionate reaction (rx 4) in the basic medium cannot be ruled out. Reaction 3 and 4 will be the competitive reactions with the reduction of Sn^{2+} to Sn^0.

$$NaBH_4 + SnCl_2 \cdot 2H_2O \longrightarrow [Sn]_{colloid} \bullet \text{ (stabilizer)} + NaBO_2 + NaCl + H_2 \quad (1)$$

$$[Sn]_{colloid} + H_2O \longrightarrow Sn(-/@)SnO_2 \bullet \text{ (stabilizer)} + H_2 \quad (2)$$

$$SnCl_2 + H_2O + 2NaBO_2 \longrightarrow SnO_2 + B_2O_3 + 2NaCl + H_2 \quad (3)$$

$$2SnCl_2 + 4NaBO_2 \longrightarrow SnO_2 + Sn + 2B_2O_3 + 4NaCl \quad (4)$$

After the synthesis is finished, NPs are precipitated using centrifugal at 8000~20000 rpm for 20~30 min and the top supernatant is decanted or saved for further centrifugal at an elevated speed. The precipitated NPs are re-dispersed into the same volume of NMP. The centrifugal is repeated 2 or 3 times and the final black slurry in the bottle is dried under vacuum and kept in desiccators.

Size, shape, morphologies and crystal-lattice fringes of nanoparticles were characterized by transmission electron microscopy (TEM; JOEL 2100F, 200kV). Chemical compositions at different locations of Sn@SnO2 nanorods were examined by energy-dispersive X-ray spectroscopy (EDS) coupled into the TEM chamber. Powder X-ray diffraction (XRD) data of samples were collected on a D/max 2200PC diffractometer (Cu Kα radiation, λ= 1.54056 Å, Rigaku, Japan). The photoluminescence (PL) properties of samples were performed at room temperature by using an Xe 900 lamp with the photon wavelength (λ_{ex}) fixed at 300 nm or 325 nm as excitation source and a photomultiplier tube detector, R928P Hamamatsu PMT, as the detector to collect the emission light (Hitachi F-4500, Japan).

Results and Discussion

MT-SPMPs show their versatilities in size, shape, morphology and crystal-structure control in the Sn-based nanohybrid synthesis as the precise kinetic parameter control at each stage during the NPs formation is coupled with the synergistic effects of the stabilizers. Figure 1B gives the stabilizers and the corresponding kinetic parameters at each stage for the synthesis of varieties of Sn-SnO_2 nanohybrids or Sn@SnO_2 NPs (R1-R6).

Temperature is both one of the most important kinetic parameters for reaction-rate control and one of the most important thermal-dynamic factors in the growth and crystal-structure control during the nanoparticle formation.[36,44] Temperatures at each stage can be flexibly controlled by MT-SPMPs. Here, experiments with two distinctly different temperatures, 27.5 ± 2.5 ^{o}C (R1) and 82.5 ± 2.5 ^{o}C (R3), for the mixing/reaction/nucleation (controlled by thermostatic tank 1) and

growth stage (controlled by thermostatic tank 2) were first performed at a flow rate of 1.75 ± 0.25 mL/min per pump, using PVP as the stabilizer as the collecting/post-annealing temperature was controlled at 27.5 ± 2.5 ^{o}C by the thermostatic tank 3.

As shown in Fig. s1a, core-shell nanorods mixed with some nanospheres are formed as observed by TEM images as the mixing/reaction, nucleation and growth temperatures are controlled at 27.5 ± 2.5 ^{o}C (R1). These nanorods can be well separated from the mixture by centrifugal at 8000~10000 rpm for 30 min (R2), as shown in Fig. 2a. Their diameter and length distributions extracted from over 65 randomly selected individual NPs are depicted in Figs. s2a and s2b. Statistics suggest that these nanorods have a diameter of 19.2 ± 2.8 nm and length of 66.2 ± 12.2 nm. The high resolution TEM (HR-TEM) image for one typical nanorod clearly reveals the core-shell structure (Fig. 2b) with a crystalline core and an amorphous shell doped with a few tiny crystalline areas (~2 nm). The lattice spacing of 0.276 nm in the core can be indexed as the tetragonal Sn (101) plane (PDF No.: 04-0673). The shell-thickness distribution extracted from over 65 randomly selected individual NPs, depicted in Fig. s2c, gives a thickness of 2.8 ± 0.2 nm, near the exciton Bohr radius of SnO_2.[25] The lattice spacing of 0.237 nm of the crystalline area in the shell possibly can be indexed as SnO_2 (200) plane (PDF No.: 41-1445). Peaks at 30.48^{o}, 31.88^{o}, 43.84^{o}, 44.82^{o}, 55.28^{o}, 62.40^{o}, 64.44^{o}, 72.78^{o} and 79.38^{o} from the XRD spectrum of these core-shell nanorods correspond to the (200), (101), (220), (211), (301), (112), (321), (411) and (312) planes of tetragonal tin. The two broad and weak peaks at 26.96^{o} and 52.06^{o} are possibly from the amorphous shells doped with the tiny crystalline areas. Note: peaks for the (110) and (211) planes of tetragonal SnO_2 should appear at about 26.96^{o} and 52.06^{o} according to the PDF No.: 41-1445. The scanning TEM image (STEM, Fig. s2d), EDS measurements on areas of the core and the shell (Fig. s2e and s2f) of one typical nanorod, the STEM image (Fig. s2g), and the Sn element mapping (Fig. s2h) of another typical nanorod suggest that these nanorods are composed of Sn-rich cores and Sn-deficient but oxygen-rich shells. Therefore, combination of HR-TEM results, XRD measurement (Fig. 2c) and the EDS measurements on some

typical nanorods indicate that cores are made of tetragonal tin and shells of amorphous SnO_2 doped with a few tiny crystalline SnO_2 areas. The nanospheres in the supernatant can be obtained by further centrifugal at 10000~12000 rpm for 30 min several times, as shown in Fig. s1b. Statistics extracted from over 110 randomly selected particles reveal these nanospheres have a uniform mean diameter of 4.0 ± 0.3 nm (Fig. s1c).

Figure 1d shows the room temperature photoluminescence (RM-PL) of the Sn@SnO_2 nanorods (λ_{ex} = 300 nm). There are 6 discernable peaks or shoulders in the spectrum, 337 nm (3.69 eV), 347 nm (3.59 eV), 403 nm (3.08 eV), 447 nm (2.77 eV), 508 nm (2.45 eV) and 525 nm (2.37 eV), implying 6 types of emission centers in the nanorods, according to previous study on tin oxides.[6,24,28,30,32,45-49] The highest peak at 347 nm, revealing a strong UV emission, can be attributed to the direct bandgap of SnO_2, suggesting that the dipole-forbidden rule (the band-edge radiative transition) was overcome in the Sn@SnO_2 nanohybrids. Evidently, with the onset absorption wavelength of tin oxide nanocrystals determined to be 346 nm (3.6 eV), the shoulder peak at 337 nm possibly is due to the effect of the enhanced free-electron concentration from the metallic tin cores on the SnO_2 shells. Thus, the unequivocal quantum-size effects and the electron density in shells can be greatly enhanced in Sn@SnO_2 nanorods due to highly crystalline metallic tin cores and a few tiny crystallinity doping amorphous SnO_2 shells with thickness near the exciton Bohr radius of SnO_2 (2.7 nm).[25-29,50] Other peaks can be possibly ascribed to some structural defects or luminescent centers of different energy levels (e.g., oxygen vacancies, tin interstitials or dangling).[30,47-49]

Interestingly, nanospheres with distinct core-shell morphology (Fig. 3a-b) can be formed as the mixing/reaction, nucleation and growth temperatures are controlled at 82.5 ± 2.5^{o}C (R3). These core-shell nanospheres give a full diameter of 13.8 ± 3.5 nm, having a core diameter of 11.0 ± 3.1 nm (Fig. s3a) and a shell thickness of 2.8 ± 0.4 nm (Fig. s3b) by measuring over 100 randomly selected particles. The HR-TEM image for one typical particle clearly reveals a highly crystalline core and an amorphous shell. XRD characterization (Fig. 3c) and HR-TEM images suggest that

their cores are made of tetragonal tin and shells of amorphous SnO_2. These Sn@SnO_2 NPs all show a symmetric and smooth mono-peak emission (Fig. 3d) centered at 475 nm (2.60 eV). This band at 475 nm has been observed in varieties of SnO_2 materials as a shoulder or weak peak, which possibly can be attributed to the electron transition mediated by defect levels in the bandgap,[24,51] or the formation of oxygen vacancies in the V_O^{++} charge state (or V_O^{++} luminescent center).[52,53] A V_O^{++} center is formed by the recombination of a surface-trapped hole with an electron in deep trap V_O^{+} (singly charged oxygen vacancy), giving a visible emission as the conduction-band electrons recombine with the V_O^{++} centers.[54] These oxygen vacancies can be created as the donor level below the conduction band and are the origin of the n-type SnO_2, formed due to the insufficient crystallization in amorphous SnO_2, according to the experimental analysis on the phase.

According to previous investigation on the main causes of ultraviolet[33] and optical[5,18,22,25-27] excitonic gains, our results indicate that more oxygen vacancies can be formed in the Sn@SnO_2 nanospheres than in the Sn@SnO_2 nanorods with luminescence centers mainly of tin interstitials. This conclusion can be well understood if we recall the related competitive reactions during the NPs formation. According to the morphology and crystal-structure difference between these nanospheres formed at high temperature and the nanorods formed at low temperature, it can be reasonably deduced that high temperature can increase reactions 2, 3 and 4 to produce more SnO_2 rapidly. Some of the rx 1 to form Sn^0, in fact, follow the rx-5, and $NaBH_4$ can decompose quickly to produce lots of B at high temperature, similar to the synthesis of Fe(B)@Fe_3O_4 NPs.[42] Thus, lots of B and B_2O_3 can be produced together with SnO_2.

$$NaBH_4 + SnCl_2{\bullet}2H_2O \longrightarrow [Sn(B)]_{colloid}{\bullet}\ (stabilizer) + NaBO_2 + NaCl + H_2 \qquad (5)$$

Since the reaction solution passes through the growing tubing very quickly and the collecting is performed at a relative low temperature, there is not sufficient time and/or energy for atoms to move to their equilibrium positions in the crystalline SnO_2. Simultaneously, lots of B_2O_3 and/or B will be trapped in the SnO_2 phase. These B atoms can compete with Sn to produce lots of oxygen vacancies that favor visible

emission. As the reaction, nucleation and growth are performed at low reaction temperature, reactions of 2, 3 and 4 can be relatively suppressed, leading to more Sn^0 formed than SnO_2. The growth of tin particles is thermodynamically controlled. In order to reduce the whole system energy, tin NPs will follow an orientated growth due to the tetragonal anisotropic structure of tin, here, preferring to (101) plane of Sn, leading to the rod shape.[25] Simultaneously, many Sn atoms can be trapped in SnO_2 phases, leading to the formation of tin interstitials. Thereby, the main causes for the blue excitonic gains in Sn@SnO_2 nanospheres and for the ultraviolet excitonic gains in Sn@SnO_2 nanorods can be reasonably deduced by their formation mechanism.

Clearly, the size dispersion of Sn@SnO_2 nanospheres seemed very broad (STDEV%: ~ 25%). Therefore, sodium citrate (TSC) of 3.3 g (11.2 mmol) and/or maleic anhydride (MA) of 0.52 g (5.3 mmol) were added into the 50 mL PVP-$SnCl_2$ aqueous solution, according to our investigation on the synergistic effect of PVP, TSC and MAH in the dispersion stabilization and size control of Fe_3O_4 and Fe(B)@ Fe_3O_4 NPs.[42,43] As expected, ultra-small nanospheres can be formed as the experiment (R4) was performed at the same reaction condition as the above Sn@SnO_2 NPs. The diameter distribution (Fig. s4a) extracted from over 120 randomly selected NPs reveals their mean diameter of 2.6 ± 0.2 nm, showing much reduced size dispersion (STDEV%: ~ 9.2%) by comparing with the above Sn@SnO_2 NPs. This result, again, suggests a synergistic effect in the controlled growth of NPs as for the Fe_3O_4 NPs.[43] The HR-TEM image of one typical particle (Fig. 4b) suggests that these nanospheres are in crystalline phases with different crystal lattices at the center and the surface. Their XRD measurement (Fig. 4e: i) reveals several distinct, sharp tetragonal Sn peaks and weak but sharp tetragonal SnO_2 peaks. As further evidenced by the crystal-lattice measurement by the HR-TEM image of one typical nanoparticle (Fig. 4b, 0.203 nm: crystal lattice of (211) plane of tetragonal Sn, PDF No: 04-0673; 0.264 nm: crystal lattice of (101) plane of tetragonal SnO_2, PDF No: 41-1445), these tiny NPs are clearly hybridized by Sn and SnO_2. However, their PL measurements show a suppressed blue emission band centered at 475 nm by comparing with those 13.8 nm Sn@SnO_2 nanospheres with the same Sn content in solutions (0.71mmol /L). The

reduced emission intensity in the tiny Sn-SnO_2 nanospheres is clearly resulted from the surface passivation by MAH and TSC and the reduced defect density according to their morphology and crystallinity.

The kinetic parameters in each reaction stage during the nanoparticle formation (e.g., the collection temperature) can be controlled much more conveniently and precisely by MT-SPMPs than by the conventional batch process, particularly for the collecting temperature that is extremely critical in the further growth control and crystallization of NPs. According to our previous synthesis condition for the amorphous cobalt NPs, the collection temperature consequently was reduced to 0-2^{o}C (R5) for improved SnO_2 contents and the enhanced defect density by suppressing the crystallization during the tiny Sn-SnO_2 nanohybrid formation. As shown in Fig. 4c-d, ultra-small Sn-SnO_2 hybrid nanospheres can be synthesized, having much smaller size and more disordered crystalline phases than those collected at 27.5 ± 2.5^{o}C. The diameter distribution extracted from over 150 randomly selected NPs (Fig. s4b) gives a mean diameter of 2.1 ± 0.3 nm with ~ 2 atomic layers deviation.

The HR-TEM image for one typical particle (Fig. 4d) reveals that the particle is made by one low crystalline component and one much disordered component. Their XRD pattern (Fig. 4e-ii) gives 3 tetragonal Sn inflection peaks at 30.28^{o} ((200) plane), 31.08^{o} ((101) plane) and 44.42^{o} (mixed (220) and (211) plane) and one distinct broad peak at 26.98^{o} (position of (110) plane in tetragonal SnO_2, PDF No: 41-1445). This result indicates that these tiny NPs are hybridized by the low-crystalline Sn component and the nearly amorphous SnO_2 component, having a higher SnO_2 content than the 2.6 nm NPs. Clearly, these ultra-small NPs collected at low temperature are not in perfect crystalline phases but full of defects. Amazingly but as expected, these ultra-small Sn-SnO_2 nanohybrids show a much more enhanced blue emission centered at 475 nm than those ultra-small 2.6 nm Sn-SnO_2 NPs and those large Sn@SnO_2 NPs, which can be ascribed to the increased SnO_2 content and the highly increased defect density according to their morphologies and crystal structures.

MT-SPMPs are also convenient to perform a sequential synthesis (i.e., *in-situ* annealing of as-synthesized, ultra-small NPs). Fig. s5a shows one typical TEM image

of NPs by *in-situ* annealing the 2.08 nm Sn-SnO_2 nanohybrids at ~90°C for more than 2 hours (R6). Surprisingly, Sn@SnO_2 NPs with distinct core-shell morphology can be formed. The size distribution extracted from over 110 randomly selected NPs suggests a mean core diameter of 9.8 ± 1.0 nm and a mean shell thickness of 1.8 ± 0.2 nm (Fig. s5b and s5c). Their XRD measurement (Fig. s5d) suggests that they are made of crystalline Sn and SnO_2. They exhibit a similar PL emission centered at 475 nm (Fig. s5e-i) as those of the 13.8 nm Sn@SnO_2 NPs (Fig. s5e-ii) and the 2.08 nm Sn-SnO_2 NPs (Fig. s5e-iii), indicating similar defects (mainly oxygen vacancies) formed in SnO_2 components during the growth of the 2.08 nm Sn@SnO_2 NPs. Their reduced PL emission by comparing with their precursors is clearly due to the reduced defect content (mainly oxygen vacancies) by the increased crystallinity and the further reducing reaction of the unconsumed reductants in the annealing process. Calculation by their geometry, the volume ratio of SnO_2 in these small Sn@SnO_2 NPs is about 39.7%, slightly less than that in the large Sn@SnO_2 NPs with amorphous SnO_2 (49.3%). However, they have almost the same mass-averaged emission intensity at 475 nm, indicating a higher defect density than that in the large Sn@SnO_2 NPs. Their higher emission at the low wavelength tail than the large Sn@SnO_2 NPs is possibly due to the size effect (small core and reduced shell thickness) and the enhanced electronic coupling from small metallic cores.

Conclusion

A new proof-of-concept strategy by coupling the synergistic effects of complex surfactants with the precise kinetic parameter control in each stage during the nanoparticle formation via simple-programmed microfluidic processes has been developed in the controlled synthesis of nanohybrids using Sn-SnO_2 and Sn@SnO_2 nanohybrids as examples. Their sizes can be well controlled from 2 nm to 14 nm, shapes from sphere to rod, morphology from component-mixed hybrid to core shell, and crystal structure from amorphous phase to crystalline phase. Particularly, SnO_2 components can be well controlled at the exciton Bohr radius range of SnO_2, and defect types and densities can be adjusted conveniently during their formation. Investigation on their microstructure-dependent photoluminescence reveals enhanced,

unequivocal quantum-size effects and interfacial electronic-coupling effects between each component, which endow them with well-controlled optical properties (nearly monotone blue emission band centered at 475 nm or unique ultraviolet emission band at 347 nm) due to the precise size, shape, morphology and crystallinity control via the newly developed synthesis strategy. Consequently, the challenging quantum dipole-forbidden rule in SnO_2 can be overcome to realize the UV emission by constructing hybrid nanorods with highly crystalline tin cores and SnO_2 shells with thickness in the exciton Bohr radius range.

Acknowledgements

This work was supported by NSFC (Grant Nos. 51371018 and 50971010), the Fundamental Research Funds for the Central Universities (YWF-11-03-Q-002), SRF and SEM from Chinese Education Ministry. The authors also appreciate Ms. Hannah Matthews in the Applied Research Center at Old Dominion University, Newport News, VA USA, for her assistance in English-proof.

References

(1) Yang, P.; Zhao, D.; Margolese, D. I.; Chmelka, B. F.; Stucky, G. D.: Generalized syntheses of large-pore mesoporous metal oxides with semicrystalline frameworks. *Nature* **1998**, *396*, 152-155.

(2) Wang, Z. L.; Song, J.: Piezoelectric Nanogenerators Based on Zinc Oxide Nanowire Arrays. *Science* **2006**, *312*, 242-246.

(3) Wang, J.; Li, W.; Wang, F.; Xia, Y.; Asiri, A. M.; Zhao, D.: Controllable synthesis of SnO_2@C yolk–shell nanospheres as a high-performance anode material for lithium ion batteries. *Nanoscale* **2014**, *6*, 3217-3222.

(4) Feng, S.; Xu, R.: New Materials in Hydrothermal Synthesis. *Acc. Chem. Res.* **2001**, *34*, 239-247.

(5) Vasiliev, R. B.; Babynina, A. V.; Maslova, O. A.: Photoconductivity of nanocrystalline SnO_2 sensitized with colloidal CdSe quantum dots *J. Mater. Chem. C* **2013**, *1*, 1005-1010.

(6) Chopra, K. L.; Major, S.; Pandya, D. K.: Transparent conductors—A status review. *Thin Solid Films* **1983**, *102*, 1-46.

(7) Grosse, P.; Schmitte, F. J.; Frank, G.; Köstlin, H.: Preparation and growth of SnO_2 thin films and their optical and electrical properties. *Thin Solid Films* **1982**, *90*, 309-315.

(8) Agekyan, V. T.: Spectroscopic properties of semiconductor crystals with direct forbidden energy gap. *Phys. Status Solidi A,* **1977**, *43*, 11-42.

(9) Yu, B.; Zhu, C.; Gan, F.: Exciton spectra of SnO2nanocrystals with surficial dipole layer. *Opt. Mater.* **1997**, *7*, 15-20.

(10) Wang, L.; Chen, Y.; Ma, J.; Chen, L.; Xu, Z.; Wang, T.: Hierarchical SnO_2 Nanospheres: Bio-inspired Mineralization, Vulcanization, Oxidation Techniques, and the Application for NO Sensors. *Scientific Reports* **2013**, *3*, 3500.

(11) Anjali, S.; Tomarb, M.; Gupta, V.: Room temperature trace level detection of NO_2 gas using SnO_2 modified carbon nanotubes based sensor,. *J. Mater. Chem.* **2012**, *22*, 23608-23616.

(12) Arnold, M. S.; Avouris, P.; Pan, Z. W.; Wang, Z. L.: Field-Effect Transistors Based on Single Semiconducting Oxide Nanobelts. *J Phys Chem B* **2003**, *107*, 659-663.

(13) Sun, C.; Karthik, K. R. G.; Stevin, S.: The role of tin oxide surface defects in determining nanonet FET response to humidity and photoexcitation. *J. Mater. Chem. C* **2014**, *2*, 940-945.

(14) Huang, H.; Liang, B.; Liu, Z.; Wang, X.; Chen, D.; Shen, G.: Metal oxide nanowire transistors *J. Mater. Chem.* **2012** *22*, 13428-13445.

(15) Kim, J. S.; Granstro¨m, M.; Friend, R. H.; Johansson, N.; Salaneck, W. R.; Daik, R.; Feast, W. J.; Cacialli, F.: Indium–tin oxide treatments for single- and double-layer polymeric light-emitting diodes: The relation between the anode physical, chemical, and morphological properties and the device performance. *J. Appl. Phys.* **1998**, *84*, 6859-6870.

(16) Heo, S. W.; Ko, Y. D.; Kim, o. S.; Moon, D. K.: Enhanced performance in polymer light emitting diodes using an indium-zinc-tin oxide transparent anode by the controlling of oxygen partial pressure at room temperature. *Journal of Materials Chemistry C* **2013**, *1*, 7009–7019.

(17) Ganapathy, V.; Kong, E.-H.; Park, Y.-C.; Jang, H. M.; Rhee, S.-W.: Cauliflower-like SnO_2 hollow microspheres as anode and carbonfiber as cathode for high performance quantum dot and dye-sensitized solar cells. *Nanoscale* **2014**, *6*, 3296-3301.

(18) Zhang, X.; Ren, H.; Tingting Wang; Zhang, L.; Li, L.; Wang, C.; Su, Z.: Controlled synthesis and magnetically separable photocatalytic properties of magnetic iron oxides@SnO_2 yolk-shell nanocapsules. *J. Mater. Chem.* **2012**, *22* 13380-13385.

(19) He, M.; Yuan, L.; Hu, X.; Zhang, W.; Shu, J.; Huang, Y.: A SnO_2@carbon nanocluster anode material with superior cyclability and rate capability for lithium-ion batteries. *Nanoscale* **2013**, *5*, 3298-3305.

(20) Jin, Y.-H.; Min, K.-M.; Seo, S.-D.; Shim, H.-W.; Kim, D.-W.: Enhanced Li Storage Capacity in 3 nm Diameter SnO_2 Nanocrystals Firmly Anchored on Multiwalled Carbon Nanotubes. *J. Phys. Chem. C* **2011**, *115*, 22062–22067.

(21) Chen, J. S.; Archer, L. A.; Lou, X. W. D.: SnO_2 hollow structures and TiO_2 nanosheets for lithium-ion batteries, . *J. Mater. Chem.* **2011**, *21*, 9912-9924.

(22) Frohlich, D.; Kenklies, R.; Helbig, R.: Band-gap assignment in SnO_2 by two-photon spectroscopy. *Phys. Rev. Lett.* **1978**, *41*, 1750-1751.

(23) Li, Y.; Yin, W.; Deng, R.; Chen, R.; Chen, J.; Yan, Q.; Yao, B.; Sun, H.; Wei, S.-H.; Wu, T.: Realizing a SnO_2-based ultraviolet light-emitting diode via breaking the dipole-forbidden rule. *NPG Asia Materials* **2012**, *4*, e30.

(24) Wang, B.; Yang, Y. H.; Yang, G. W.: Growth mechanisms of SnO_2/Sn nanocables. *Nanotechnology* **2006**, *17*, 4682-4688.

(25) Liu, L. Z.; Li, X. X.; Wu, X. L.; Chen, X. T.; Chu, P. K.: Growth of tin oxide nanorods induced by nanocube-oriented coalescence mechanism. *Appl. Phys. Lett.* **2011**, *98*, 133102.

(26) Xi, G.; Ye, J.: Ultrathin SnO_2 Nanorods: Template- and Surfactant-Free Solution Phase Synthesis, Growth Mechanism, Optical, Gas-Sensing, and Surface Adsorption Properties. *Inorg. Chem.* **2010**, *49*, 2302-2309.

(27) Sefardjella, H.; Boudjema, B.; Kabir, A.; Schmerber, G.: Structural and photoluminescence properties of SnO_2 obtained by thermal oxidation of evaporated Sn thin films. *Current Applied Physics* **2013**, *13*, 1971-1974.

(28) Xu, X.; Zhuang, J.; Wang, X.: SnO_2 Quantum Dots and Quantum Wires: Controllable Synthesis, Self-Assembled 2D Architectures, and Gas-Sensing Properties. *J Am Chem Soc* **2008**, *130*, 12527-12535.

(29) Wang, J. X.; Liu, D. F.; Yan, X. Q.; Yuan, H. J.; Ci, L. J.; Zhou, Z. P.; Gao, Y.; Song, L.; Liu, L. F.; Zhou, W. Y.; Wang, G.; Xie, S. S.: Growth of SnO_2 nanowires with uniform branched structures. *Solid State Communications* **2004**, *130*, 89-94.

(30) Bansal, S.; Pandya, D. K.; Kashyap, S. C.; Haranath, D.: Growth ambient dependence of defects, structural disorder and photoluminescence in SnO_2 films deposited by reactive magneton sputtering. *J. Alloy Comp.* **2014**, *583*, 186-190.

(31) Hu, J. Q.; Ma, X. L.; Shang, N. G.; Xie, Z. Y.; Wong, N. B.; Lee, C. S.; Lee, S. T.: Large-scale rapid oxidation synthesis of SnO_2 nanoribbons. *J. Phys. Chem. B* **2002**, *106*, 3823-3826.

(32) Luo, S.; Chu, P. K.; Liu, W.; Zhang, M.; Lin, C.: Origin of low-temperature photoluminescence from SnO_2 nanowires fabricated by thermal evaporation and annealed in different ambients. *Appl. Phys. Lett.* **2006**, *88*, 183112.

(33) Yang, H. Y.; Yu, S. F.; Lau, S. P.; Tsang, S. H.; Xing, G. Z.; Wu, T.: Ultraviolet coherent random lasing in randomly assembled SnO_2 nanowires *Appl. Phys. Lett.* **2009**, *94*, 241121.

(34) Kar, A.; Stroscio, M. A.; Dutta, M.; Kumari, J.; Meyyappan, M.: Observation of ultraviolet emission and effect of surface states on the luminescence from tin oxide nanowires. *Appl. Phys. Lett.* **2009**, *94*, 101905.

(35) Song, Y.; Zhang, T.; Yang, W. T.; Albin, S.; Henry, L. L.: Fine Crystal Structure Transition of Cobalt Nanoparticles Formed in a Microfluidic Reactor. *Crystal Growth & Design* **2008**, *8*, 3766-3772.

(36) Song, Y.; Henry, L. L.; Yang, W. T.: Stable Cobalt Amorphous Nanoparticles Formed by an In-situ Rapid Cooling Microfluidic Process *Langmuir* **2009**, *25* 10209-10217.

(37) Song, Y.; Henry, L. L.: Nearly Monodispersion CoSm Nanoparticles Synthesized by a Microfluidic reactor. *Nanoscale Res. Lett.* **2009**, *4*, 1130-1134.

(38) Song, Y.; Sun, S.; Zhang, T.; Jin, P.; Han, L.: Synthesis of Worm and Chain-like Nanoparticles by a Microfluidic Reactor Process. *J. Nanopart. Res.* **2010**, *12*, 2689-2697.

(39) Song, Y.; Jin, P.; Zhang, T.: Microfluidic Synthesis of Fe Nanoparticles. *Mater. Lett.* **2010**, *64*, 1789-1792.

(40) Song, Y.; Ding, J.; Wang, Y.: Shell Dependent Evolution of Optical and Magnetic Properties of Co@Au Core-shell Nanoparticles. *J Phys Chem C* **2012**, *116*, 11343-11350

(41) Song , Y.; Wang, Y. H.; Ji, S.; Ding, J.: Shell-Driven Fine Structure Transition in Co@Au Core-shell Nanoparticles. *Nano-Micro Lett.* **2012**, *4*, 235-242.

(42) Song, Y.; Ji, S.; Song, Y.-J.; Li, R.; Ding, J.; Shen, X.; Wang, R.; Xu, R.; Gu, X.: In-situ Redox Microfluidic Synthesis of Core-Shell Nanoparticles and their Long-term Stability. *J. Phys. Chem. C* **2013**, *117*, 17274-17284.

(43) Song, Y.; Wang, R.; Rong, R.; Ding, J.; Liu, J.; Li, R.; Liu, Z.; Li, H.; Wang, X.; Zhang, J.; Fang, J.: Synthesis of Well-dispersed Aqueous-phase Magnetite Nanoparticles and their Metabolism as MRI Contrast Agent for Reticuloendothelial System *European Journal of Inorganic Chemistry* **2011**, 3303-3313.

(44) LaMer, V. K.; Dinegar, R. H.: Theory, Production and Mechanism of Formation of Monodispersed Hydrogols. *J. Am. Chem. Soc.* **1950**, *72*, 4847-4854.

(45) Davazoglou, D.: Optical properties of SnO_2 thin films grown by atmospheric pressure chemical vapour deposition oxiding $SnCl_4$. *Thin Solid Films* **1997**, *302*, 204-213.

(46) Luo, S.; Fan, J.; Liu, W.; Zhang, M.; Song, Z.; Lin, C.; Wu, X.; Chu, P. K.: Synthesis and low-temperature photoluminescence properties of SnO_2 nanowires and nanobelts. *Nanotechnol.* **2006**, *17*, 1695–1699.

(47) Jeong, J.; Choi, S.-P.; Chang, C. I.; Shinb, D. C.; Park, J. S.; Lee, B.-T.; Park, Y.-J.; Song, H.-J.: Photoluminescence properties of SnO_2 thin films grown by thermal CVD. *Solid State Communications* **2003**, *127*, 595–597.

(48) Rani, S.; Roy, S. C.; Karar, N.; Bhatnagar, M. C.: Structure, microstructure and photoluminescence properties of Fe doped SnO_2 thin films. *Solid State Communications* **2007**, *141*, 214-218.

(49) Gu, F.; Wang, S. F.; Lü, M. K.; Cheng, X. F.; Liu, S. W.; Zhou, G. J.; Xu, D.; Yuan, D. R.: Luminescence of SnO_2 thin films prepared by spin-coating method. *J. Cryst. Growth* **2004**, *262*, 182-185.

(50) Cheng, B.; Russell, J. M.; Shi, W.; Zhang, L.; Samulski, E. T.: Large-scale, solution-phase growth of single-crystalline SnO_2 nanorods. *J. Am. Chem. Soc.* **2004**, *126*, 5873-5972.

(51) Nagano, M.: Growth of SnO_2 whiskers by VLS mechanism. *Journal of Crystal Growth* **1984**, *66*, 377-379.

(52) Das, S.; Kar, S.; Chaudhuri, S.: Optical properties of SnO_2 nanoparticles and nanorods synthesized by solvothermal process. *J. Appl. Phys.* **2006**, *99*, 114303.

(53) Liu, L. Z.; Xu, J. Q.; Wu, X. L.; Li, T. H.; Shen, J. C.; Chu, P. K.: Optical identification of oxygen vacancy types in SnO_2 nanocrystals. *Appl. Phys. Lett.* **2013**, *102*, 031916.

(54) Seo, H. W.; Bae, S. Y.; Park, J.; Yang, H.; Park, K. S.; Kim, S.: Strained gallium nitride nanowires *J. Chem. Phys.* **2002**, *116*, 9492.

Figure Captions

Figure 1 (a) Experiment setup of microtubing-based, simple-programmed microfluidic processes (MT-SPMPs): (1) and (2), syringe pumps for reducing-agent solution and metal-salt solution; (3) and (4), microtubing coils for pre-heating reducing-agent solution and metal-salt solution with the temperature controlled by thermostatic tank 1; (5), three-way mixer for reaction between reducing-agent solution and metal-salt solution; (6), microtubing coil for nucleation and nanoparticle growth with temperature controlled by thermostatic tank 2; (7), nanoparticle collector with temperature controlled by thermostatic tank 3, where the growth is terminated at a designated temperature. (b) Synthesis routes and reaction conditions of MT-SPMPs for Sn-SnO_2 nanohybrids with different morphology and crystal structure: R1, Sn@SnO_2 nanorods mixed with some nanospheres; R2, Sn@SnO_2 nanorods with shell thickness of 2.8 ± 0.2 nm obtained by centrifugal of the solution from R1; R3, Sn@SnO_2 NPs (crystalline core: 11.0 ± 3.1 nm; amorphous shell: 2.8 ± 0.4 nm); R4, 2.1 nm Sn-SnO_2 NPs; R5, 2.6 nm Sn-SnO_2 NPs; R6, Sn@SnO_2 NPs (crystalline core: 9.8 ± 1.0 nm; shell: 1.8 ± 0.2 nm). T_R: reaction temperature, T_C: collection temperature. D: Diameter, L: Length, T: Thickness, D_C: core diameter, D_S: shell thickness.

Figure 2 (a) TEM image, (b) HR-TEM image, (c) XRD and (d) photoluminescence spectrum of Sn@SnO_2 nanorods (diameter: 13.8 nm; length: 66 nm; shell thickness: 2.8 ± 0.2 nm) obtained by centrifugal (8000-10000 rpm, 30 min) of the nanoparticle solution as synthesized at 27.5 ± 2.5°C using PVP as stabilizer. Crystal lattices in b, 0.237 nm: SnO_2 (200) plane; 0.276 nm: Sn (101) plane.

Figure 3 (a) TEM image, (b) HR-TEM image, (c) XRD and (d) photoluminescence (PL) spectrum of Sn@SnO_2 nanodots synthesized at 82.5 ± 2.5°C only using PVP as stabilizer. Crystal lattice in b, 0.289 nm: Sn (200) plane.

Figure 4 (a) TEM image and (b) HR-TEM image of 2.6 ± 0.2 nm Sn-SnO_2 nanohybrids synthesized at 80°C and collected at 27.5 ± 2.5°C using PVP, TSC and MAH complex stabilizers; (c) TEM image and (d) HR-TEM image of 2.1 ± 0.3 nm Sn-SnO_2 nanohybrids synthesized at the reaction temperature of 82.5 ± 2.5°C and the collection temperature of 0~2°C using PVP, TSC and MAH complex stabilizers; (e) XRD of 2.6 nm (i) and 2.1 nm (ii) Sn-SnO_2 nanohybrids; (f) photoluminescence spectra of 2.6 ± 0.2 nm (i) and 2.1 ± 0.3 nm (ii) Sn-SnO_2 nanohybrids by comparing with Sn@SnO_2 nanodots (iii) (core: 11.0 ± 3.1 nm; shell: 2.8 ± 0.4 nm) synthesized at 82.5 ± 2.5°C only using PVP as the stabilizer. Solutions for PL measurement are controlled at the same concentration of 0.71 mM (mmol/L) based on tin content. The intensities in f are standardized by assuming the intensity of the sample (a) as 100. Crystal lattices: 0.208 nm in b, Sn (220) plane; 0.203 nm in d, Sn (211) plane; 0.264 nm in d: SnO_2 (101) plane.

Figure 1

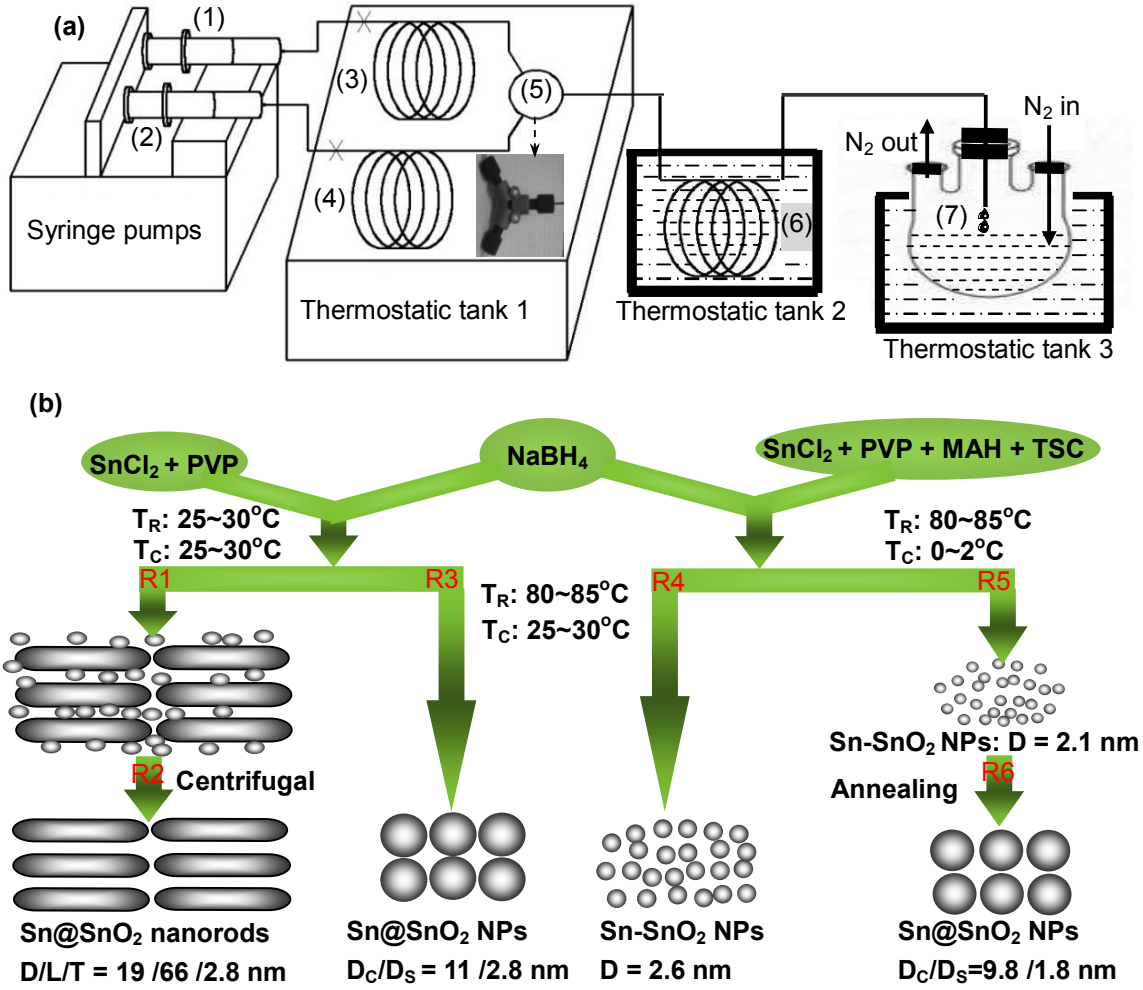

Figure 2

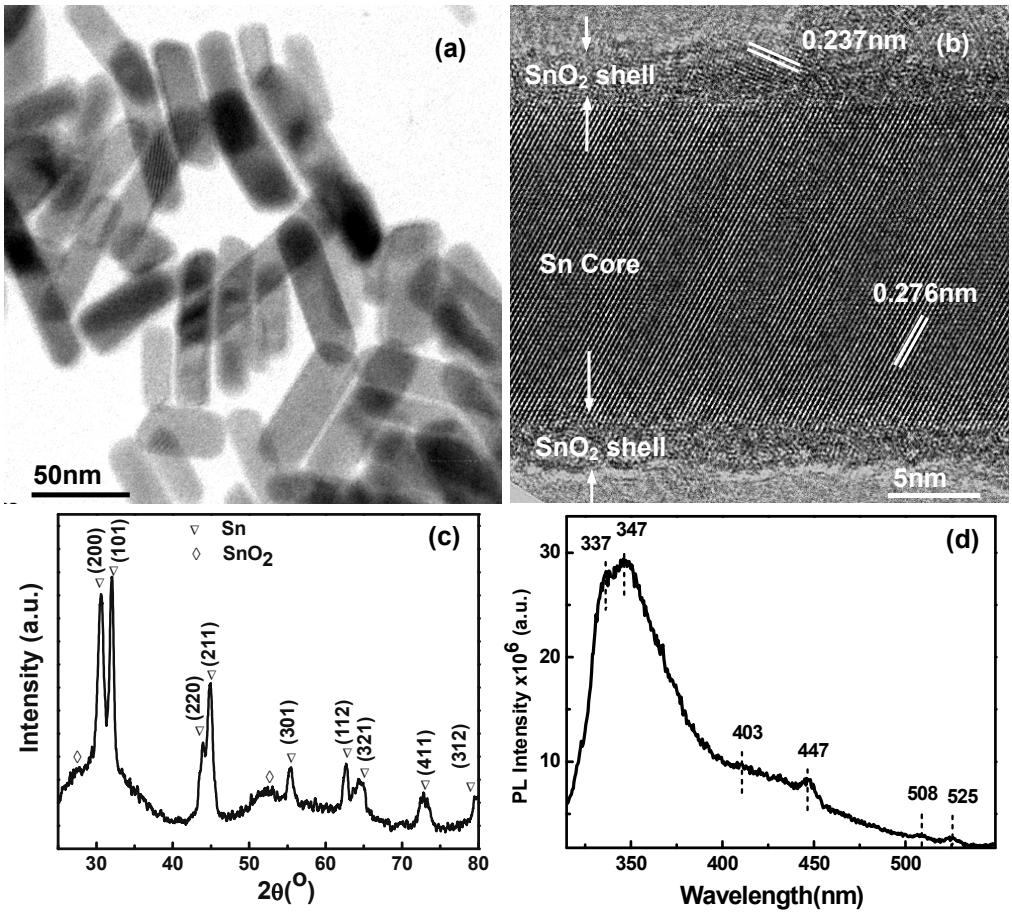

Figure 3

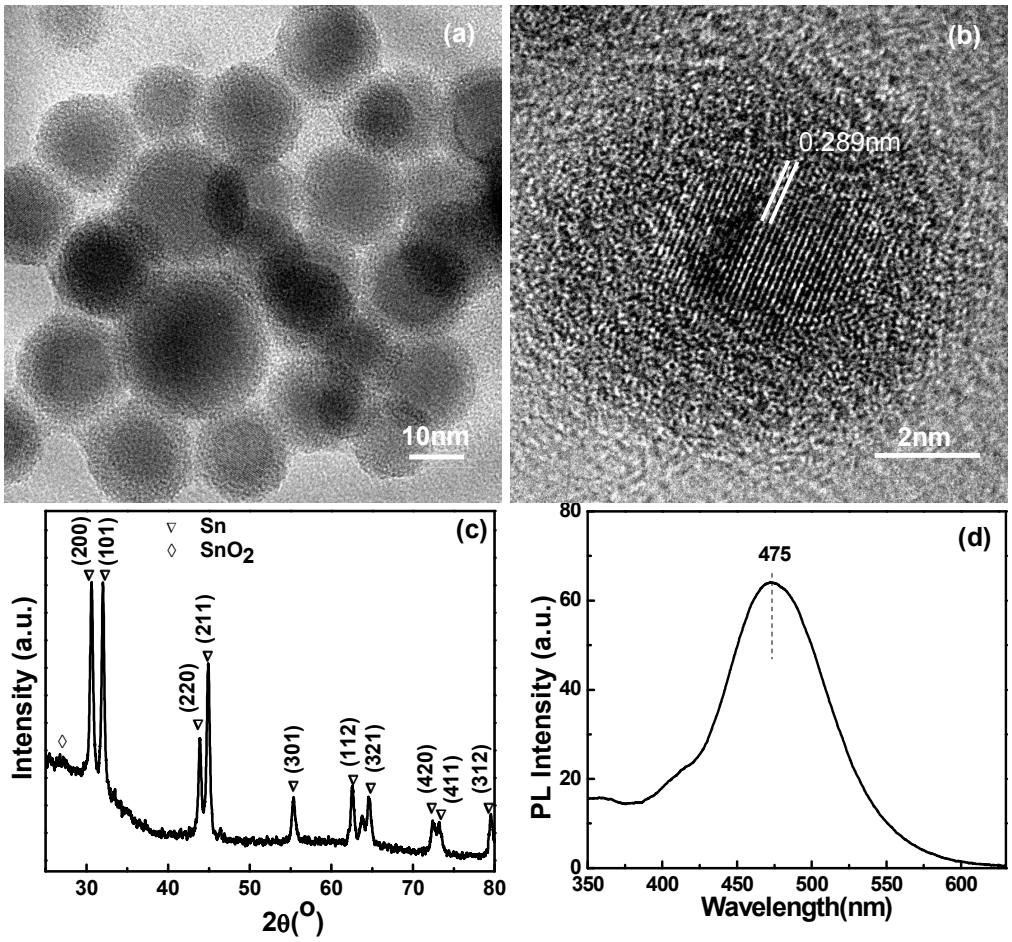

Figure 4

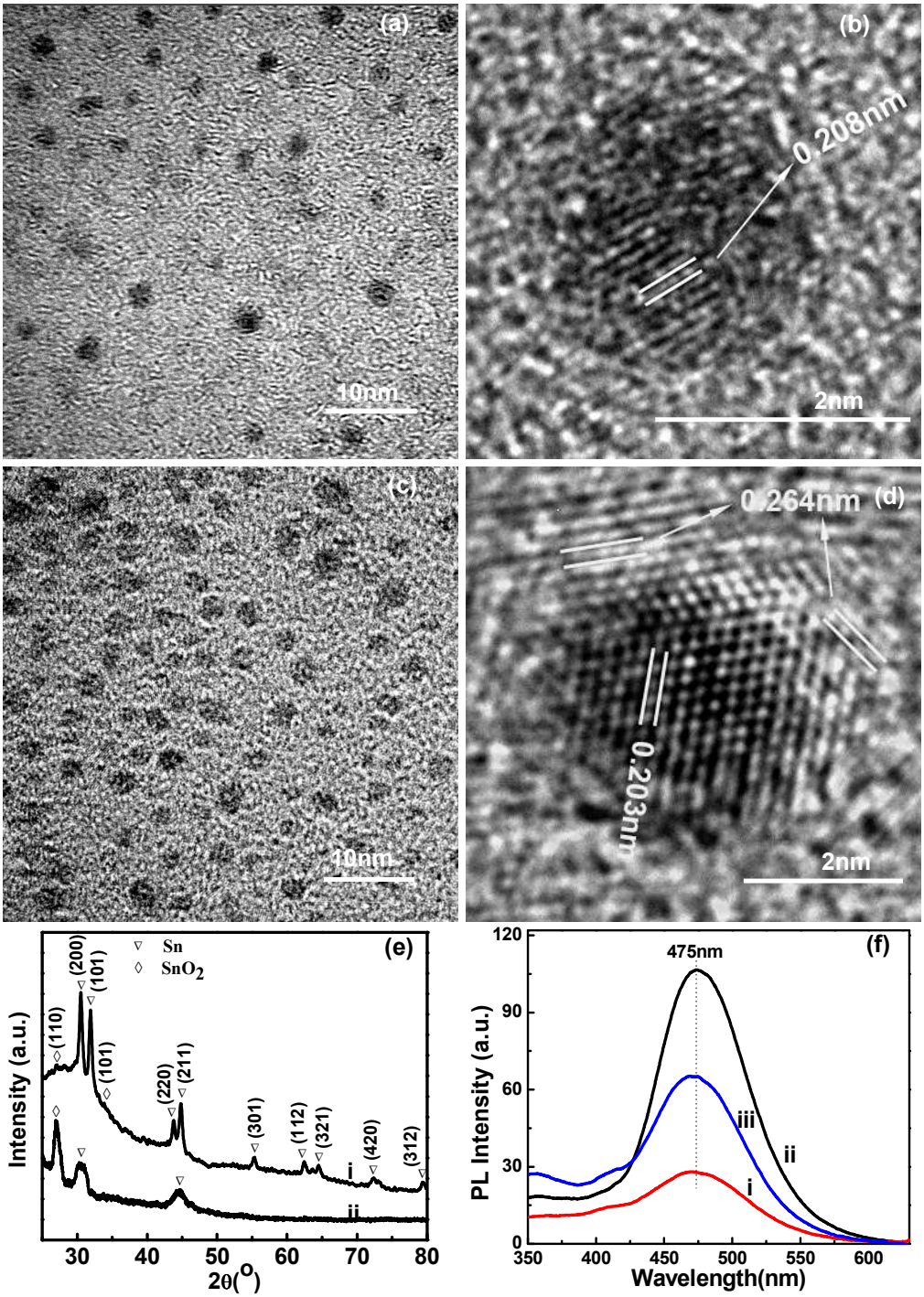

Graphic Abstract

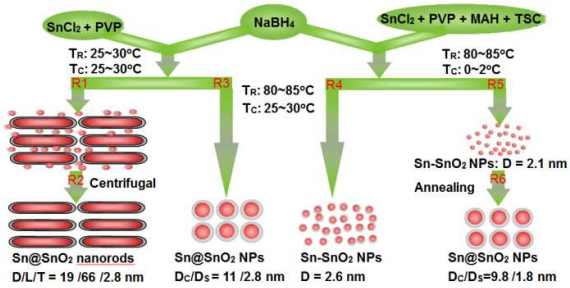

Simple programmed microfluidic processes show the precise morphology and crystal structure controlled synthesis of nanohybrids using Sn-SnO_2 nanohybrids as models